STRUCTURAL SCIENCE
CRYSTAL ENGINEERING
MATERIALS

ISSN 2052-5206

Cation distribution in $Cu_2ZnSnSe_4$, Cu_2FeSnS_4 and $Cu_2ZnSiSe_4$ by multiple-edge anomalous diffraction

Daniel M. Többens,* Galina Gurieva, Sara Niedenzu, Götz Schuck, Ivo Zizak and Susan Schorr

Structure and Dynamics of Energy Materials, Helmholtz-Zentrum Berlin für Materialien und Energie, Hahn-Meitner-Platz 1, Berlin, 14165, Germany. *Correspondence e-mail: daniel.toebbens@helmholtz-berlin.de

Received 5 June 2020
Accepted 6 October 2020

Edited by M. de Boissieu, SIMaP, France

Keywords: synchrotron; anomalous diffraction; semiconductor; MEAD.

CCDC references: 2035694; 2035695

Supporting information: this article has supporting information at journals.iucr.org/b

Multiple-Edge Anomalous Diffraction (MEAD) has been applied to various quaternary sulfosalts belonging to the adamantine compound family in order to validate the distribution of copper, zinc and iron cations in the structure. Semiconductors from this group of materials are promising candidates for photovoltaic applications. Their properties strongly depend on point defects, in particular related to cation order–disorder. However, Cu^{+}, Zn^{2+} and Fe^{2+} have very similar scattering factors and are all but indistinguishable in usual X-ray diffraction experiments. Anomalous diffraction utilizes the dependency of the atomic scattering factors f' and f'' of the energy of the radiation, especially close to the element-specific absorption edges. In the MEAD technique, individual Bragg peaks are tracked over an absorption edge. The intensity changes depending on the structure factor can be highly characteristic for Miller indices selected for a specific structural problem, but require very exact measurements. Beamline KMC-2 at synchrotron BESSY II, Berlin, has been recently upgraded for this technique. Anomalous X-ray powder diffraction and XAFS compliment the data. Application of this technique confirmed established cation distribution in $Cu_2ZnSnSe_4$ (CZTSe) and Cu_2FeSnS_4 (CFTS). In contrast to the literature, cation distribution in $Cu_2ZnSiSe_4$ (CZSiSe) is shown to adopt a highly ordered wurtz-kesterite structure type.

1. Introduction

The quaternary sulfosalt semiconductors $Cu_2B^{II}C^{IV}X_4$ (B^{II} = Zn, Fe; C^{IV} = Sn, Ge, Si; X = S, Se) have drawn wide attention for their potential applications in many fields. Depending on their band gaps these materials are interesting for thin film solar cells, high-temperature thermoelectric materials and nonlinear optics (Schnabel *et al.*, 2017; Guo *et al.*, 2012; Heinrich *et al.*, 2014; Rosmus *et al.*, 2014). $Cu_2ZnSnSe_4$ (CZTSe) is an alternative candidate for absorber layers in thin film solar cells due to its narrow bad gap of 1.0 eV and high absorption coefficient of >104 cm^{-1} (León *et al.*, 2014; Ahn *et al.*, 2010). Cu_2FeSnS_4 (CFTS) with a band gap of 1.3 eV can also be used for this purpose and in addition has photocatalytic properties (Baláž *et al.*, 2017). $Cu_2ZnSiSe_4$ (CZSiSe), which has a band gap of 2.2 eV (Yao *et al.*, 1987; Guc *et al.*, 2014) is proven to be a promising nonlinear optical material for use in the infrared region (Rosmus *et al.*, 2014).

It is well established that cation arrangement in the respective structure is a parameter crucial for the electronic properties of quaternary sulfosalts. However, the cations involved are often isoelectronic or nearly so. In the compounds examined here, only Sn^{4+} is distinct and its loca-

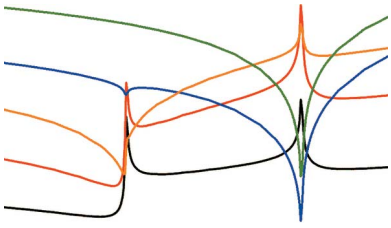

tion in the crystal structure can easily be identified by routine laboratory X-ray diffraction. Cu^{+} and Zn^{2+} on the other hand are isoelectronic cations. As a result, their X-ray scattering characteristics, expressed by the atomic form factor f, are nearly identical by conventional means. Standard X-ray diffraction thus cannot reliably distinguish these two elements. Fe^{2+} has four electrons fewer, but this only amounts to a difference of about 15% in scattering power. Considering the possibility of partial occupation of structural sites, mixed occupation and strong correlation with displacement parameters, this difference is often not enough for a reliable identification.

Anomalous diffraction has been used to overcome this problem (Hodeau *et al.*, 2001). As the atomic form factor changes at the absorption edges of the respective elements, isoelectronic cations can be distinguished from diffraction data taken with radiation of appropriate energies. Ideally, it should be possible to simultaneously refine multiple datasets with different wavelengths, and from this to directly derive the site occupancy factors. In practice, the results of this procedure were found to be unstable (Többens, Gunder *et al.*, 2016). This is in largely due to the comprehensive nature of diffraction analysis. As the diffraction pattern is defined by the complete structure, all aspects of the crystal structure have to be refined simultaneously. This makes the method very powerful, but also can lead to strong correlation effects. In particular, atomic scattering power, site occupation factors, displacement parameters and small atomic displacements from symmetry-breaking phase transitions tend to be highly correlated with each other, resulting in high uncertainties for the individual values. A method that depends only on one aspect of the crystal structure is superior in this case.

Multiple-Edge Anomalous Diffraction (MEAD) is such an approach. This method calls for measuring the energy dependency of the intensity of selected Bragg peaks *hkl* around the X-ray absorption edge of a chemical element. For all elements, the anomalous components change in the same way, with the real anomalous scattering factor f' having a minimum at the energy of the edge and the imaginary anomalous scattering factor f'' increasing discontinuously. In the structure factor

$$F_{hkl}(E) = \sum_n \mathrm{occ}_n[f_0 + f'(E) + if''(E)]_n \exp[2\pi i(hx_n + ky_n + lz_n)],$$

however, the relation between atomic scattering factor and intensity is modulated by the position (x,y,z) of the atom and the Miller index *hkl* of the specific Bragg reflection in complex ways. It is thus often possible to find individual Bragg reflections that show the effect of particular changes in the structure particularly strongly. Measuring the energy dependency for these peaks instead of just the intensity at a single or a few energies adds another layer of selectivity, as only sites containing the specific element can affect the energy dependency.

To the best of our knowledge, the term MEAD (Multiple-Edge Anomalous Diffraction) has only been coined recently (Collins *et al.*, 2015) in a study trying to distinguish cobalt and manganese, but the method has been in use at least since 2007 (Collins *et al.*, 2007). An incomplete variant has actually been used to study the Cu–Zn distribution in CZTS (Nozaki *et al.*, 2012), confirming the known kesterite over stannite structure type. This last work, however, did use only a small number of different energies, all at the low-energy site of the Cu *K* absorption edge. While this choice is reasonable in terms of reduction of measuring time and avoiding the increased background from fluorescence above the absorption edge, it limits the expressiveness of the results. Richter *et al.* (2018) applied the method to amplify the sensitivity of the Bragg peak intensity to small atom displacements by tuning the scattering factor of strontium at its *K*-edge. It should also be noted that as far as data collection is concerned the method is very similar to the well known Diffraction Anomalous Fine Structure (DAFS) and Diffraction Anomalous Near-Edge Structure (DANES) techniques. It is thus unsurprising that very similar approaches have been developed as variations of DAFS (Ersen *et al.*, 2003) and DANES (Lefevre *et al.*, 2016). However, DAFS/DANES generally aims at analysing the local structure by making use of the deviations of f' and f'' from the theoretical curve, which in turn are derived from the fine structure of the X-ray absorption spectrum. MEAD aims at the properties of the average crystal structure and can thus safely neglect the fine structure of the intensity. This significantly reduces the level of difficulty, making MEAD much more accessible for non-specialists.

2. Experimental

2.1. Sample synthesis

Cu_2FeSnS_4 (CFTS) used here is a sample used in a previous analysis (Schorr *et al.*, 2007), the iron-rich, zinc-free end-member in the solid-solution series CFTS-CZTS. The structure was found to be stannite type using neutron powder diffraction, with no significant deviation of the cation distribution from complete order.

$Cu_2ZnSnSe_4$ (CZTSe) used here was also used in a previous analysis (Többens, Gurieva, *et al.*, 2016). It was shown to be slightly off-stoichiometric, with an experimental composition of $Cu_{1.96}Zn_{1.04}Sn_{0.99}Se_4$, and to contain only traces (0.1±0.05 wt% each) of orthorhombic Cu_2Se_4 and γ-selenium. The sample had been carefully annealed at 100°C and has the highest degree of Cu/Zn order of any sample used in that study. The order parameter of the Cu/Zn order–disorder transition associated with the symmetry reduction to $I\bar{4}$, the transition from disordered into ordered kesterite structure, has been determined as 0.61 (6) by anomalous X-ray diffraction.

$Cu_2ZnSiSe_4$ (CZSiSe) was synthesized as part of the $Cu_2Zn(Si_{1-x}Ge_x)Se_4$ series (Niedenzu *et al.*, 2019, 2018). The quaternary main phase is slightly off-stoichiometric, its composition was determined as $Cu_{1.935}Zn_{0.975}Si_{1.029}Se_4$ by wavelength-dispersive X-ray spectroscopy using an electron microprobe system. Small amounts of two secondary phases were found in the sample, ZnSe and $Cu_{3-y}Si_ySe_2$, both contributing less than 1 wt% of the sample. $Cu_{3-y}Si_ySe_2$ was

not found in the diffraction pattern here, instead Bragg peaks indicating the presence of a small amount of an unidentified third phase was found instead. In addition, a small fraction of Fe_2O_3 was found, which we assume to be a later contamination. The structure of $Cu_2ZnSiSe_4$ has successfully been refined from X-ray powder diffraction as wurtz-stannite type, in agreement with prior single-crystal analysis of the compound (Gurieva *et al.*, 2015). The same orthorhombic structure type was found for the entire Si-rich part of the $Si_{1-x}Ge_x$ solid solution series.

Additional characterizations conducted on the samples are described in the aforementioned publications.

2.2. Anomalous X-ray analysis

Energy-dependent X-ray analysis was carried out on the KMC-2 beamline at BESSY II, HZB (Helmholtz-Zentrum Berlin für Materialien und Energie, 2016). The energy of the radiation provided by the Si–Ge (111) double-crystal monochromator (Erko *et al.*, 2001) is calibrated using an instrument-inherent table matching experimental position of the X-ray absorption edges of various metal foils (including Fe, Cu, Zn) against tabulated values (Wong, 2018). The energy bandwidth of the monochromator is 1/4000. Intensity stabilization of the primary beam was made by controlling the pitch of the second monochromator crystal, using a SIS2900 D-MOSTAB (SIS GmbH) monochromator stabilizer. All experiments were conducted at ambient conditions.

EXAFS data were collected at the KMC-2 XANES station in transmission geometry, using multiple layers of finely ground sample on Kapton adhesive tape. A reference foil of the respective metal was simultaneously measured using a second ionization chamber behind the main one in order to provide an internal standard for the absorption-edge energy. Data collection and treatment were conducted using established procedures, *e.g.* Zhang *et al.* (2020).

Anomalous diffraction data for powder diffraction analysis and MEAD were collected at the KMC-2 diffraction station in symmetric reflection geometry, using finely ground powder on a rotating zero-background silicon sample holder.

Full powder diffraction sets of $Cu_2ZnSiSe_4$ were collected at energies of 8048 eV (λ = 1.5406 Å, equivalent to Cu $K\alpha_1$), 8965 eV (below Cu K absorption edge) and 9645 eV (below Zn K).

Data for MEAD analysis were collected in energy ranges ±500 eV around the absorption edge, with a step size of 5 eV in the region ±100 eV around the absorption edge and a step size of 10 eV outside of this range. An area sensitive gas detector (Vantec 2000, Bruker AXS) was used. This did allow multiple peaks to be observed simultaneously in a 2θ-range of 11°. This detector model does not allow for energy discrimination, giving rise to increased background from fluorescence at energies above the absorption edges. The resulting negative effect on counting statistics was compensated for by increased data collection times, up to 150 s for each individual frame.

For CZTSe and CFTS, the low-angle Bragg peaks 002, 101 and 110 have been measured; they are close enough to allow data collection with only one detector position centered at the center of the group. For CZSiSe, the low-angle region containing 110, 101, 011, 111 and 200 was measured under the same conditions.

3. Data analysis

3.1. XAFS spectroscopy

XAFS data were processed using *ATHENA* [version 0.9.6 in the *Demeter* package; Ravel & Newville, 2005]. Radiation energies were calibrated using collected data for metal foils (Wong, 2018). The offset of the experimental energies from literature data was found to be −4.7 eV for Zn in CZSiSe, −2.6 eV for Zn in CZTSe, −2.5 eV for Fe in CFTS, −7.5 eV for Cu in CZSiSe, −5.0 eV for Cu in CZTSe and −5.1 eV for Cu in CFTS.

3.2. Rietveld refinement

Rietveld analysis of the structure of $Cu_2ZnSiSe_4$ was done using *FullProf.2k* (Version 6.30; Rodriguez-Carvajal & Roisnel, 1998). Symmetric Thompson–Cox–Hastings pseudo-Voigt functions were used for the peak shape. Background was modeled by linear interpolation between positions with little contribution from Bragg peaks. Two known minor phases were considered by Rietveld refinement and a peak at Q = 2.38 Å^{-1} was excluded. All three powder diffraction data sets collected at different energies were refined jointly with identical structural parameters; to correct for minor position errors, zero-point offsets and the wavelength for the two higher energies were refined. Preferred orientation of a fraction of the main compound along [110] and [010] was modeled using the March–Dollase multi-axial model implemented in the software. The final refinement was made in the same way for both the stoichiometric and the experimental composition of the phase, resulting in insignificant differences only.

3.3. Multiple-edge anomalous diffraction (MEAD)

3.3.1. Treatment of experimental data. The 2D data of the area detector were numerically integrated into 1D powder diffraction data, normalized to the average monitor count of the energy scan and transformed from diffraction angles 2θ into momentum space Q, resulting in a constant peak position independent of the radiation wavelength. Intensities of the Bragg peaks were fitted [*Fityk* (version 0.9.3); Wojdyr, 2010] using linear background and Gaussian peak shape with constant width for any given Miller index. Peak intensities were subsequently corrected for the transformation into Q space by application of a factor $4\arcsin(Q\lambda/4\pi)/Q$. Energy-dependent absorption by air in the 90 cm gap between monitor counter and detector was also corrected for (Hubbell, 2004). It should be noted that these two previous corrections only affect a smooth, monotonous slope of the intensity with radiation energy and are thus fairly uncritical for the quality of the results. Absorption by the sample itself was corrected by dividing observed intensities by the linear absorption coefficient μ, which is the appropriate correction for symmetric

reflection geometry (Richter *et al.*, 2018; Maslen, 2006). Linear absorption coefficients for this were calculated using stoichiometric composition and tabulated values for X-ray mass attenuation coefficients (Hubbell, 2004) and atomic masses (Meija *et al.*, 2016). As the absolute value of the correction is not needed, knowledge of the real packed density of the sample is not necessary. Prior to application, μ was shifted by the difference between the tabulated energy of the respective absorption edge of the pure element (Merritt, 2020) and the experimental one as shown by the fluorescent background. Tables of experimental intensities and correction curves are provided as supporting information. The resulting MEAD curves were then compared to simulated data for different structural models.

3.3.2. Simulation of MEAD curves. Energy-dependent curves of the intensities of powder diffraction peaks were calculated using the simulation mode in *FullProf.2k* based on the published crystal structures of kesterite-type CZTSe (Többens, Gurieva *et al.*, 2016), stannite- type CFTS (Bonazzi *et al.*, 2003) and wurtz-kesterite-type CZSiSe (Gurieva *et al.*, 2015), all taken from the Inorganic Crystal Structure Database (ICSD, 2019). The structural data were generally kept unchanged with the values given in the literature, and were only modified according to demands of the models under test. In most cases this only required changing occupation factors of the cations. In the case of CZTSe, the high-symmetry anion position with $x = y$ was also tested in addition to the published low-symmetry position with $x \neq y$; this did not have a significant influence on the results. In the case of CZSiSe, some of the tested cation occupation patterns required a reduction of the overall symmetry. This symmetry reduction was applied only to the occupancies, while retaining the published higher symmetry for all atomic positions and Debye–Waller factors. Tools from the Bilbao Crystallographic Server (Aroyo *et al.*, 2006; Kroumova *et al.*, 1999) were used for this.

Fullprof's internally tabulated coefficients for the $\sin\theta/\lambda$ dependent part of the atomic scattering factors were used. The energy-dependent factors f' and f'' of the scattering factors were interpolated from tabulated data (Merritt, 2020) according to the theoretical approximation developed by Cromer and Liberman (Cromer, 1983; Cromer & Liberman, 1981). The menial task of creating an energy-dependent series of otherwise identical *Fullprof* input files with different values for wavelength and anomalous scattering factors and the subsequent re-sorting of the calculated *hkl* intensity output was conducted using a small set of Windows batch scripts and a simple program we call *MEADmaker*. *MEADmaker* is freely available from the corresponding author.

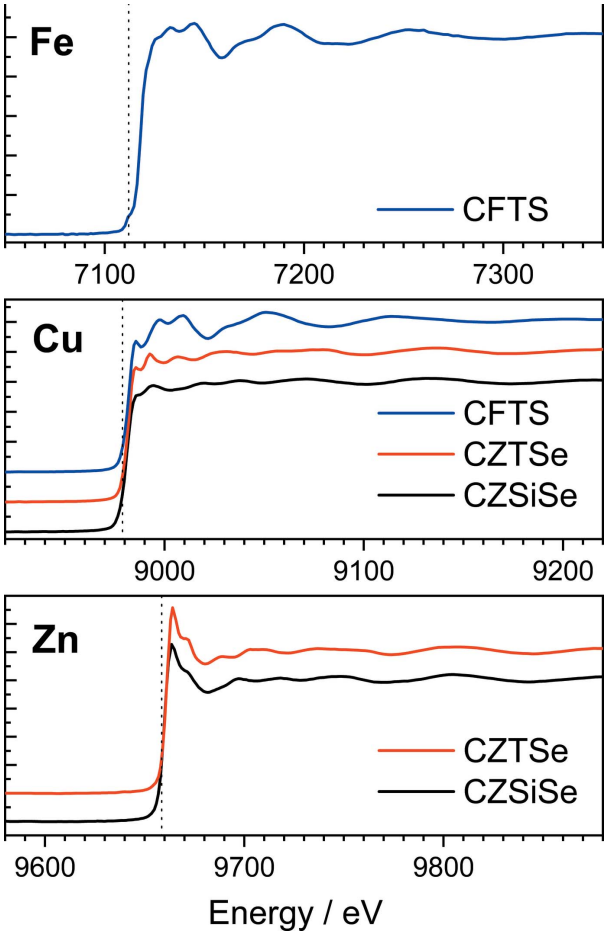

Figure 1
XAFS curves of the samples used herein. Ideal positions of the absorption edges are indicated by dotted lines.

4. Results

4.1. XAFS

X-ray absorption (XAFS) data are shown in Fig. 1. It should be possible to use these data to calculate sample-specific experimental curves of the X-ray absorption factor μ as well as the anomalous components f' and f'' of the atomic scattering factors (Dreier *et al.*, 1983). However, this did not provide any significant advantage over the use of general tabulated data for the MEAD analysis. As is well known, the fine structure of the absorption curve contains information about the local structure of the respective element. As this is not analyzed in MEAD the theoretically calculated average curve is sufficient. Of importance is the shift in the position of the absorption edge that is introduced by the crystal structure. In general, this has little effect, as the changes in μ or f' and f'' with energy are not very steep. But for data points very close to the edge this might result in them being treated as above the edge while being in fact below the edge (or *vice versa*), resulting in artificial spikes at the absorption edge. To avoid these, the tabulated data have to be shifted accordingly. This does not require high-quality XAFS data, though, the fluorescence background of the diffraction pattern was found to be sufficient.

4.2. Cu_2FeSnS_4

The iron-containing compound Cu_2FeSnS_4 (CFTS) is called stannite when appearing as the mineral and is thus the name giver for the stannite structure type. This structure derives from the cubic ZnS sphalerite structure by cations ordering in

layers containing Fe^{2+}–Sn^{4+} alternating with layers containing Cu^{+} only. This results in a doubling of the *c* lattice parameter and a symmetry reduction to $I\bar{4}2m$. However, Cu^{+} and Fe^{2+} are nearly isoelectronic and thus hard to distinguish by usual X-ray diffraction experiments. It was thus surprising to realize that none of the CFTS structure refinements deposited in the Inorganic Crystal Structure Database ICSD had employed techniques sensitive to this difference. Stannite has conclusively been shown to indeed adopt the stannite structure using neutron powder diffraction (Schorr *et al.*, 2007); however, vexingly, the results of this study never made it into the ICSD [although it is in PCD (Villars & Cenzual, 2019)]. For our simulations we used a structure that was included in the database (Bonazzi *et al.*, 2003).

If hypothetically the positions of Fe^{2+} would be switched with half of the Cu^{+} cations, in the resulting structure layers containing Cu^{+}–Sn^{4+} would alternate with layers containing Cu^{+}–Fe^{2+}. This cation arrangement is called the kesterite type (Schorr, 2011). In space group $I\bar{4}2m$, symmetry in this arrangement forces Cu^{+}–Fe^{2+} disorder within the second layer. Cation ordering results in a symmetry reduction into $I\bar{4}$. However, the MEAD curves of disordered and ordered kesterite type are very similar and for some classes of Bragg peaks, *e.g.* 002, identical. The energy dependency of this Bragg peak (Fig. 2) at the absorption edges clearly confirms the stannite structure type, while being utterly different from what would be expected for a kesterite type.

4.3. $Cu_2ZnSnSe_4$

Whether CZTSe and its sulfide analog CZTS adopt the kesterite or the stannite type had long been disputed, but eventually the question was settled by neutron powder diffraction (Schorr, 2011; Schorr *et al.*, 2007). Both compounds adopt the kesterite type cation distribution. As with CFTS, this is also immediately obvious by MEAD. Essentially, this analysis is identical to the previous one, with the obvious exception that instead of the Fe edge the Zn edge was measured. The structures and the corresponding simulated MEAD curves are very similar. As for CFTS, the low-angle Bragg peaks 002, 101 and 110 have been measured. At the bottom of Fig. 3 is displayed the observed and calculated curves for the 110 Bragg peak. The MEAD peak at the *K*-edge that would be expected for stannite type is entirely absent. The peak at the Zn *K*-edge is positive instead of negative, in agreement with kesterite over stannite. Peak 002, not shown, also confirms this.

Both experimental curves shown in Fig. 3 exhibit a feature not predicted by any of the theoretical simulations, a shift of the overall intensity upwards for higher intensities. This is an experimental artifact: with increasing energies and decreasing wavelength Bragg peaks shift to lower diffraction angles, resulting in reduction of the diameter of the Debye ring projected on the detector. Even at low diffraction angles the area detector at KMC-2 does not cover the whole Debye ring, only a section. With increasing energy, fractions of the Debye

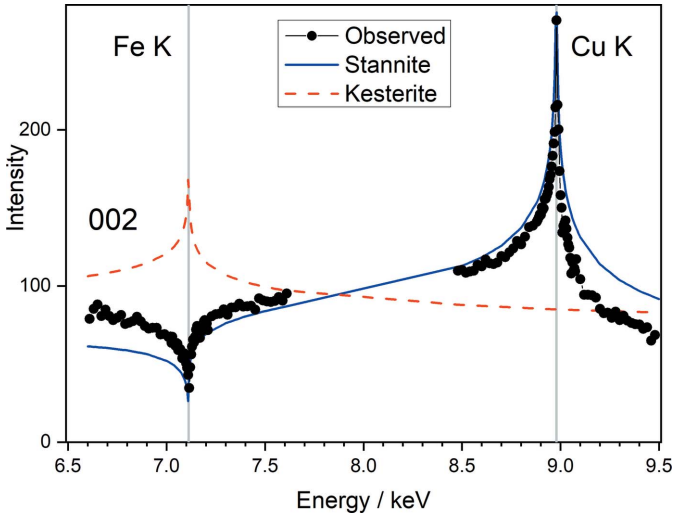

Figure 2
MEAD curves of Cu_2FeSnS_4 powder at the *K*-edges of Fe and Cu for the Bragg peak with Miller index 002. All intensity curves have been scaled to an average of 100, without offset.

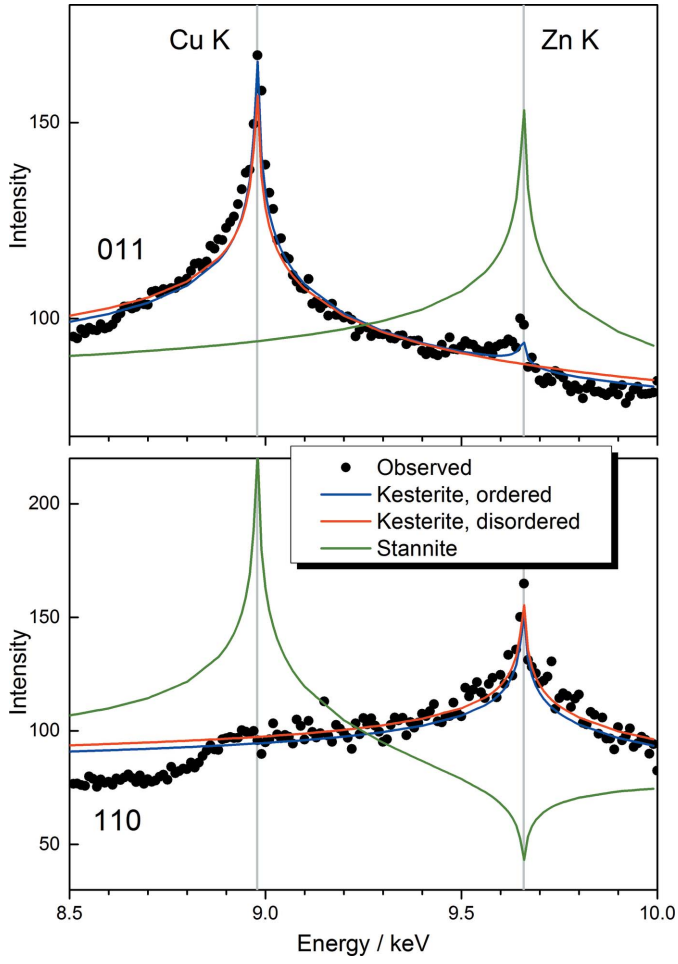

Figure 3
MEAD curves of $Cu_2ZnSnSe_4$ powder at the *K*-edges of Cu and Zn for the Bragg peaks with Miller indices 011 (top) and 110 (bottom). All intensity curves have been scaled to an average of 100, without offset. The observed shift of the intensity level at ≃8.6 keV and ≃8.8 keV is an artifact discussed in the text.

ring cross the edge of the detector from outside the observation range into the observed range. This happened here with a particularly large grain (the so-called 'rock in the dust'), which happened to contain domains in reflection position. This can be seen clearly from the raw 2D data frames (Fig. S1). It would have been easy to fix this by either increasing or decreasing the boundaries of the integration range. We left it in, as experimenters should be aware of the possibility of this effect. It is easily distinguishable from real features of the MEAD curve, as it has no relation to the energy of the absorption edge.

In addition to the cation ordering resulting in the stannite–kesterite distinction, in kesterite structures additional ordering within the Cu–Zn layer is common (Többens, Gurieva *et al.*, 2016). As mentioned before, the appearance of this ordering results in a reduction of the symmetry from space group $I\bar{4}2m$ to $I\bar{4}$. However, in the kesterite structure all atoms are located on special Wyckoff positions, leading to very high pseudosymmetry of the structure. As a result, the effects of this order on the intensity of the Bragg peaks is very small. The use of powder samples intensifies this, as symmetry-breaking reflections overlap perfectly. This is something not overcome by measuring the energy dependency. The MEAD curve of Bragg peak 011 (Fig. 3, top) shows the high degree of order in this sample only by a very small peak at the Zn *K*-edge.

4.4. $Cu_2ZnSiSe_4$

In contrast to the two previous compounds, the structure of $Cu_2ZnSiSe_4$ (CZSiSe) does not derive from the cubic sphalerite form of ZnS, but from the hexagonal wurtzite form. The cation distribution is described unanimously as wurtz-stannite (Gurieva *et al.*, 2015; Niedenzu *et al.*, 2018; Schafer & Nitsche, 1974). The lower orthorhombic symmetry of the structure results in a much lower degree of peak overlap and the potential cation ordering schemes give rise to a rich variety of MEAD curves (Fig. 4).

At one extreme Cu and Zn could potentially by randomly disordered [Fig. 4(*b*)], which would result in very uniform behavior, with all characteristic peaks showing a reduction of intensity at the absorption edges.

The published wurtz-stannite structure [Fig. 4(*a*)] in space group $Pmn2_1$ has located Zn on a 2*a* site (0,*y*,*z*) and Cu on a general 4*b* site. This is a natural assumption, as it is the only distribution that allows complete cation order within this symmetry. This distribution results in intensity maxima of the 011 and 200 peaks at the Zn edge. Note that the scale for this plot is different, as the predicted intensity changes are far higher than in any other case.

If in $Pmn2_1$ the 2*a* site is assumed to be occupied by Cu, conversely the 4*b* site is occupied by 50% Cu and 50% Zn, randomly distributed over the symmetry-equivalent sites [Fig. 4(*c*)]. This crystal structure would be a disordered wurtz-kesterite type. The resulting MEAD curves are generally characterized by a strong decrease in intensity at one absorption edge and very little change at the other, with the respective edge depending on the Miller indices.

Further fully ordered cation distributions would result in symmetry reduction. The geometric relations of the three symmetry elements *m*, *n* and 2_1 are in such a way that always two of these elements generate the third. Symmetry reduction thus necessarily leads to monoclinic symmetries. For clarity of comparison we selected for all cases the same orientation of the unit cell as in the orthorhombic structure, with $a > b > c$. This results in non-standard settings for the monoclinic space groups, $Pm11$, $P1n1$ and $P112_1$.

In space group $P1n1$ [Fig. 4(*d*)], the 4*b* site occupied by Cu in the published structure splits into two independent 2*a* sites. This allows exchanging the Zn with Cu from one of these sites. Which one does not matter, as the two options are just inverse absolute orientations. The structure resulting from this is a fully ordered wurtz-kesterite structure. Characteristic is the behavior of the MEAD curve of the 110 Bragg peak, which increases at both absorption edges, while retaining some intensity increase in the energy range between the edges; we will call this 'twin peaks' in the following. The same behavior is found for the combined peak from 101 and $\bar{1}01$. These two

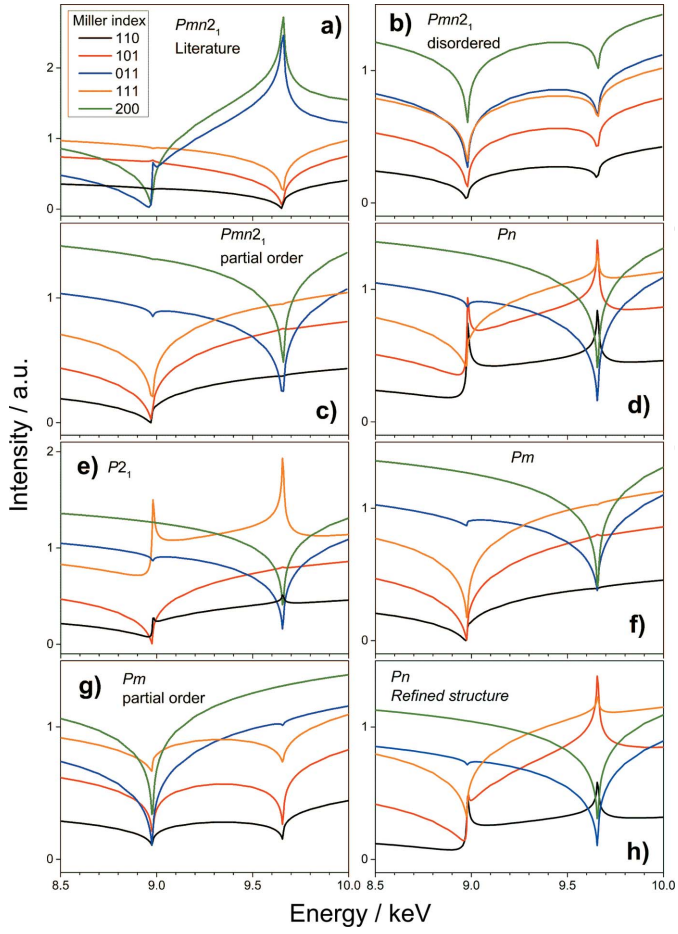

Figure 4
Simulated MEAD curves of various Cu/Zn arrangements in the structure of $Cu_2ZnSiSe_4$ for five selected Bragg peaks. The coloring scheme (see Fig. 4*a*) is the same as used for the experimental data in Fig. 5.

Bragg peaks are symmetrically independent in this space group, but still coincide in a powder pattern perfectly due to the lattice symmetry. Fortunately, their individual energy dependency is very similar, so that the sum peak retains the behavior of the individual peaks. It is worth pointing out the very significant differences between the ordered wurtz-kesterite [Fig. 4(*d*)] and the disordered one [Fig. 4(*c*)]. This is in stark contrast to the situation in the tetragonal kesterites.

If 2_1 is the symmetry element retained, again the 4*b* site splits into two independent 2*a* sites [Fig. 4(*e*)]. The alternative fully ordered Cu–Zn distribution resulting from this again gives rise to the characteristic twin peaks, but here for the 111 Bragg peak. Again this peak is fully superimposed with another peak, $\bar{1}11$. While the energy dependence of $\bar{1}11$ is quite different for this structure, it is also weaker; the 111 peak dominates the sum signal.

The final monoclinic option, retaining the *m* mirror plane, is slightly more complicated [Fig. 4(*g*)]. As with the other two options, the 4*b* site occupied by Cu in the published structure splits into two independent twofold sites, 2*c* in space group *Pm*11. But the Zn site also splits into two independent sites, 1*a* and 1*b*. This does not matter as far as alternative fully ordered structures are concerned, as the Zn from both sites has to be switched with the Cu from one of the 2*c* sites. This gives rise to a strong decrease of intensity at only one of the absorption edges for the characteristic peaks, very similar to the behavior predicted for the partially ordered distribution in $Pmn2_1$. A distinction between these two structures would not be possible by any of the five peaks selected as characteristic for this analysis. However, this cation distribution would result in significant intensity of Bragg peaks forbidden by n_y (*h*0*l* with *h*+*l* = even only), but allowed in a space group without glide symmetry elements. The 201 peak would be expected to be particularly strong, again with a twin peak dependency. Unfortunately, this Bragg peak is close to the much stronger 020. The 001 peak on the other hand remains quite weak. Luckily this turned out to be irrelevant.

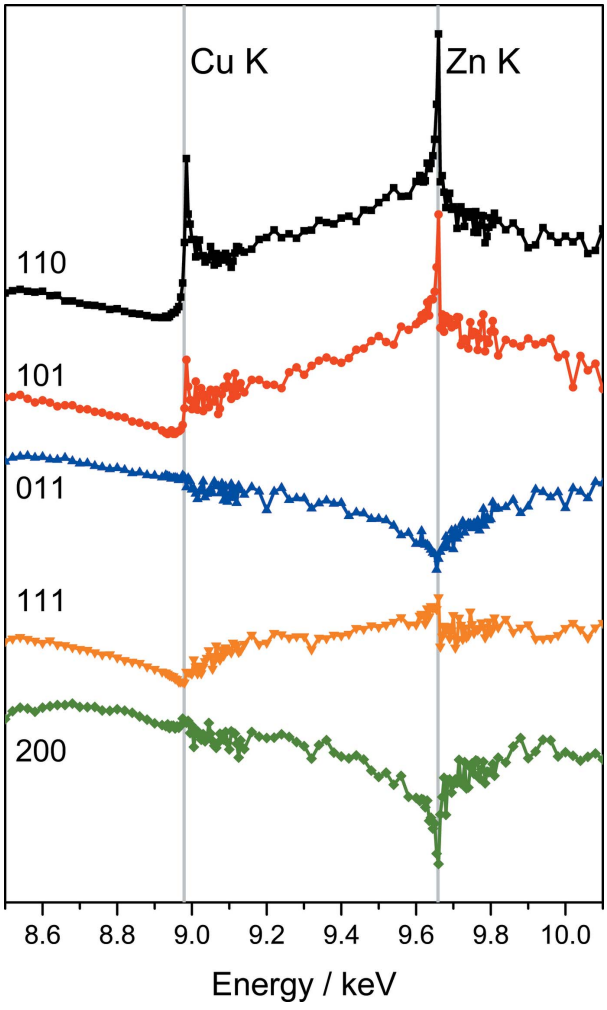

Figure 5
Experimental MEAD curves of $Cu_2ZnSiSe_4$ powder at the *K*-edges of Cu and Zn for five selected Bragg peaks indicated by their Miller indices. Absolute intensity offsets are shifted, but otherwise unscaled. Upon comparison with the simulation in Fig. 4 it is obvious that Fig. 4(*d*) is the correct solution.

Space group *Pm*11 allows for two additional partially disordered structures [Fig. 4(*f*)], where the Zn from either one of the sites 1*a* or 1*b* is replaced by Cu and one of the 2*c* sites is occupied by 50% Cu and 50% Zn in random distribution. This would result in minima at the Cu edge only for the 200 peak and the 011 and $0\bar{1}1$ combined signal, while for the remaining three peaks a 'twin dip' behavior with minima at both edges would be expected. The two different 2*c* sites give rise to structures with distinctly different cation distribution. However, they are all but indistinguishable by our quintet of (not completely) characteristic peaks. Again, 001 or 201, peaks forbidden in the higher symmetry, could be used for distinction.

In summary, MEAD analysis of selected characteristic peaks allows clear and unambiguous distinction between all potential cation distributions in this compound. Upon comparing the experimental values (Fig. 5) with these simulations it is obvious that the cation distribution in the published structure is incorrect. The only ordering scheme compatible with the observations is the one presented in Fig. 4(*d*), requiring a symmetry reduction into monoclinic space group *Pn*. The cation arrangement in this structure is such that wurtz-kesterite rather than wurtz-stannite is the correct name of this structure type.

Subsequently, the crystal structure was refined, as discussed in the following. Based on the final structure, the MEAD curve shown in Fig. 4(*h*) was calculated. In particular one should note the signal of the 101 Bragg peak at the Cu edge, which is much weaker than in Fig 4(*d*). This agrees with the observations (Fig. 5). It is a result of the partial disorder of the real structure.

4.4.1. Structure refinement of $Cu_2ZnSiSe_4$. Refinement of the crystal structure of $Cu_2ZnSiSe_4$ in the correct space group *Pn* was carried out using both the ideal composition of the overall sample (results in Table S1 in supporting information) and the experimentally determined off-stoichiometric composition $Cu_{1.935}Zn_{0.975}Si_{1.029}Se_4$ of the phase (Table 1). No significant difference between those two approaches was found for the refined values of any structural parameter.

Table 1
Structural parameters of off-stoichiometric $Cu_2ZnSiSe_4$ with experimental composition $Cu_{1.935}Zn_{0.975}Si_{1.029}Se_4$.

Lattice parameters: a = 7.824322 (16), b = 6.730621 (12), c = 6.450758 (15) Å, β = 90.0659 (2)°, V = 339.7131 (12) Å^3.

Atom	x	y	z	U_{iso} (Å^2)	s.o.f.
Cu1	0.7489 (15)	0.8286 (8)	0.6379 (10)	0.0130 (4)	0.902 (30)
Zn1	0.7489 (15)	0.8286 (8)	0.6379 (10)	0.0130 (4)	0.098 (30)
Cu2	0.7423 (15)	0.1802 (7)	0.1240 (12)	0.0130 (4)	0.062 (30)
Zn2	0.7423 (15)	0.1802 (7)	0.1240 (12)	0.0130 (4)	0.877 (30)
Cu3	0.0036 (17)	0.6507 (3)	0.1264 (11)	0.0159 (7)	0.971
Si3	0.0036 (17)	0.6507 (3)	0.1264 (11)	0.0159 (7)	0.029
Si4	0.00	0.3273 (6)	0.625	0.0078 (9)	1.00
Se5	−0.0042 (13)	0.6439 (2)	0.5005 (9)	0.0106 (4)	1.00
Se6	−0.0028 (13)	0.3203 (2)	−0.0208 (9)	0.0126 (4)	1.00
Se7	0.7405 (14)	0.8315 (6)	0.0096 (9)	0.0056 (7)	1.00
Se8	0.7598 (14)	0.1714 (6)	0.5070 (11)	0.0151 (9)	1.00

Residuals were also only insignificantly lower for the off-stoichiometric composition. This is due to the small degree of off-stoichiometry. It also makes it hard to determine which atomic sites are affected.

The Rietveld refinement was carried out using three powder diffraction patterns simultaneously; one each at the Cu and Zn edges and one far away from the edges (see *Experimental*). This allowed the refinement of three individual occupation factors for each site and, thus, experimental determination of the positions of Cu, Zn, Si and vacancies. Starting from a refinement with completely free distribution of all cations over all four sites, consecutively unphysical solutions have been eliminated: negative site occupancy factors, occupancy factors >1 and deviations from the experimentally determined overall composition of the phase. The resulting structure (Table 1) has the fourth site fully occupied by silicon; this had already been established in the literature, as the lighter silicon can be easily distinguished from copper and zinc in the usual X-ray diffraction experiments. As the silicon site is not directly affected by the symmetry reduction from orthorhombic to monoclinic, there is no reason to expect this to be erroneous. Furthermore, bond valence analysis shows that as a result of short interatomic distances this site is unsuitable for zinc or copper, but is the only really suitable site for silicon. The phase is slightly silicon-rich; however, the aforementioned process of consecutive elimination of unphysical results leads to the extra silicon occupying site 3. Besides the small fraction of silicon, site 3 was found to be occupied exclusively by copper, and to be fully occupied. Due to its off-stoichiometry, the sample contains a significant number of vacancies. These were found to be located exclusively on site 2, the zinc site. Site 1, the other copper site, is again fully occupied.

The distribution of copper and zinc between sites 1 and 2 has the potential for occupational disorder by cation exchange. Complete disorder would render the symmetry reduction unnecessary. This structure could potentially retain space group $Pmn2_1$ of the wurtz-stannite model given in the literature. Due to the cation distribution in this case the correct name of the structure would be 'disordered wurtz-kesterite'. As in kesterite, in wurtz-kesterite the possibility for partial ordering exists. This can be described by the same order–disorder (OD) parameter calculated from the site occupations as OD = (Cu1+Zn2 − Zn1−Cu2) / (Cu1+Zn2 and Zn1+Cu2) ranging between 0 and 1 (Többens, Gurieva *et al.*, 2016). Our sample turned out to be highly ordered, with OD = 0.88 (5). The value varies with the treatment of the displacement parameters of the atoms, but even so occupation factors vary only by a few percent and always remain within the range of estimated uncertainty.

5. Summary

The final Rietveld refinement of the correct structure of $Cu_2ZnSiSe_4$ yields an overall χ^2 factor of 6.3 for the three equally weighted diffraction patterns. Individual residuals are R_{wp} = 0.049, χ^2 = 11.2 for pattern 1 (at Cu $K\alpha_1$ wavelength), R_{wp} = 0.043, χ^2 = 5.3 for pattern 2 (taken at the Cu K edge), and R_{wp} = 0.010, χ^2 = 2.0 for pattern 3 (taken at the Zn K edge). Note the effect the increased background due to fluorescence has on the residuals, resulting in an illusory higher quality. In comparison, an otherwise equal refinement using the wurtz-stannite structure given in the literature yields comparably low residuals, if anisotropic peak broadening is used to model the effects of the small, unresolved monoclinic split. A test refinement resulted in an overall χ^2 factor of 8.6. Individual residuals were R_{wp} = 0.052, χ^2 = 12.5 for pattern 1 (at Cu $K\alpha_1$ wavelength), R_{wp} = 0.058, χ^2 = 9.5 for pattern 2 (taken at the Cu K edge) and R_{wp} = 0.012, χ^2 = 3.1 for pattern 3 (taken at the Zn K edge).

While the correct structure results in lower, better quality indicators, these differences are quite small, making them quite unconvincing when arguing that the widely accepted model is fundamentally incorrect. Direct inspection of the diffraction pattern, often a very powerful approach, is also of limited value here (Fig. 6): the splitting of peaks caused by the

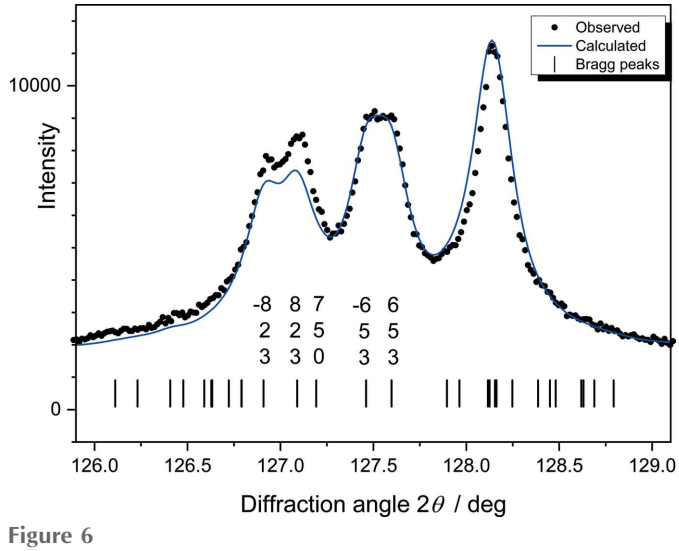

Figure 6
Section of the refined powder diffraction pattern of $Cu_2ZnSiSe_4$ with clearest signs of peak splitting caused by symmetry reduction to monoclinic. In orthorhombic cell 653 and $\bar{6}53$ would coincide, as would 823 and $\bar{8}23$.

very small deviation of the monoclinic angle of the unit cell from 90° might reasonably be explained by anisotropic broadening or neighboring peaks.

Multiple-edge anomalous diffraction, on the other hand, provides a very clear and convincing picture, leaving no doubt about the correct solution. This is possible because, unlike a comprehensive method like Rietveld refinement, the analysis with MEAD specifically picks aspects that are sensitive only to the problem at hand. This maximizes the observed changes and reduces the potential influence of correlations with other structural parameters. While measurements are quite demanding and require special instrumentation, the simulation of the expected results is straightforward, simple and not resource-intensive. It is thus an option that should always be kept in mind.

Acknowledgements

This work was made possible by allocation of synchrotron radiation beamtime at the diffraction instrument at KMC-2 beamline at BESSY II, Helmholtz-Zentrum Berlin für Materialien und Energie (HZB). Open access funding enabled and organized by Projekt DEAL.

References

Ahn, S., Jung, S., Gwak, J., Cho, A., Shin, K., Yoon, K., Park, D., Cheong, H. & Yun, J. H. (2010). *Appl. Phys. Lett.* **97**, 021905

Aroyo, M. I., Perez-Mato, J. M., Capillas, C., Kroumova, E., Ivantchev, S., Madariaga, G., Kirov, A. & Wondratschek, H. (2006). *Z. Kristallogr.* **221**, 15–27.

Baláž, P., Baláž, M., Sayagués, M. J., Eliyas, A., Kostova, N. G., Kaňuchová, M., Dutková, E. & Zorkovská, A. (2017). *Crystals*, **7**, 367.

Bonazzi, P., Bindi, L., Bernardini, G. P. & Menchetti, S. (2003). *Can. Mineral.* **41**, 639–647.

Collins, B. A., Chu, Y. S., He, L., Haskel, D. & Tsui, F. (2015). *Phys. Rev. B*, **92**, 224108.

Collins, B. A., Zhong, Y. C., Chu, Y. S., He, L. & Tsui, F. (2007). *J. Vac. Sci. Technol. B*, **25**, 999–1003.

Cromer, D. T. (1983). *J. Appl. Cryst.* **16**, 437–437.

Cromer, D. T. & Liberman, D. A. (1981). *Acta Cryst.* A**37**, 267–268.

Dreier, P., Rabe, P., Malzfeldt, W. & Niemann W. (1983). Proc. Int. Conf. on EXAFS and Near Edge Structure, 13–17th September 1982, Frascati, Italy, edited by A. Bianconi, L. Incoccia and S. Stipcich, pp. 378–380. Springer.

Helmholtz-Zentrum Berlin für Materialien und Energie (2016). *J. Large-Scale Res. Facilities*, **2**, A49.

Erko, A., Packe, I., Gudat, W., Abrosimov, N. & Firsov, A. (2001). *Nucl. Instrum. Methods A*, **467**, 623–626.

Ersen, O., Pierron-Bohnes, V., Tuilier, M. H., Pirri, C., Khouchaf, L. & Gailhanou, M. (2003). *Phys. Rev. B*, **67**, 094116.

ICSD (2019). ICSD is available at FIZ Karlsruhe at http://www.fiz-karlsruhe.de/icsd.html

Guc, M., Levcenko, S., Dermenji, L., Gurieva, G., Schorr, S., Syrbu, N. & Arushanov, E. (2014). *J. Alloys Compd.* **587**, 393–397.

Guo, Q. J., Ford, G. M., Yang, W. C., Hages, C. J., Hillhouse, H. W. & Agrawal, R. (2012). *Sol. Energy Mater. Sol. Cells*, **105**, 132–136.

Gurieva, G., Levcenko, S., Kravtsov, V., Nateprov, A., Irran, E., Huang, Y., Arushanov, E. & Schorr, S. (2015). *Z. Kristallogr. Cryst. Mater.* **230**, 507–511.

Heinrich, C. P., Day, T. W., Zeier, W. G., Snyder, G. J. & Tremel, W. (2014). *J. Am. Chem. Soc.* **136**, 442–448.

Hodeau, J. L., Favre-Nicolin, V., Bos, S., Renevier, H., Lorenzo, E. & Berar, J. F. (2001). *Chem. Rev.* **101**, 1843–1867.

Hubbell, J. H. & Seltzer, S. M. (2004). X-Ray Mass Attenuation Coefficients. NIST Standard Reference Database 126.

Kroumova, E., Perez-Mato, J. M., Ivantchev, S., Madariaga, G., Aroyo, M. I., Kirov, A. K. & Wondratschek, H. (1999). *Acta Cryst.* A**55**, 574–574.

Lefevre, C., Thomasson, A., Roulland, F., Favre-Nicolin, V., Joly, Y., Wakabayashi, Y., Versini, G., Barre, S., Leuvrey, C., Demchenko, A., Boudet, N. & Viart, N. (2016). *J. Appl. Cryst.* **49**, 1308–1314.

León, M., Levcenko, S., Serna, R., Bodnar, I., Nateprov, A., Guc, M., Gurieva, G., Lopez, N., Merino, J., Caballero, R., Schorr, S., Perez-Rodriguez, A. & Arushanov, E. (2014). *Appl. Phys. Lett.* **105**, 061909.

Maslen, E. N. (2006). *International Tables for Crystallography*, Vol. C, pp. 599–608.

Meija, J., Coplen, T. B., Berglund, M., Brand, W. A., De Bievre, P., Groning, M., Holden, N. E., Irrgeher, J., Loss, R. D., Walczyk, T. & Prohaska, T. (2016). *Pure Appl. Chem.* **88**, 265–291.

Merritt, E. A. (2020) *X-ray Anomalous Scattering.* Biomolecular Center, University of Washington. Available at http://skuld.bmsc.washington.edu/

Niedenzu, S., Gurieva, G. & Schorr, S. (2018). *IEEE 7th World Conf. Photovoltaic Energy Conversion (WCPEC)*, 3290–3293.

Niedenzu, S., Gurieva, G. & Schorr, S. (2019). *Thin Solid Films*, **669**, 625–628.

Nozaki, H., Fukano, T., Ohta, S., Seno, Y., Katagiri, H. & Jimbo, K. (2012). *J. Alloys Compds*, **524**, 22–25.

Ravel, B. & Newville, M. (2005). *J. Synchrotron Rad.* **12**, 537–541.

Richter, C., Zschornak, M., Novikov, D., Mehner, E., Nentwich, M., Hanzig, J., Gorfman, S. & Meyer, D. C. (2018). *Nature Commun.* **9**, 178.

Rodriguez-Carvajal, J. & Roisnel, T. (1998). *IUCr Commission for Powder Diffraction Newsletter*, No. 20, pp. 35–36.

Rosmus, K. A., Brant, J. A., Wisneski, S. D., Clark, D. J., Kim, Y. S., Jang, J. I., Brunetta, C. D., Zhang, J. H., Srnec, M. N. & Aitken, J. A. (2014). *Inorg. Chem.* **53**, 7809–7811.

Schafer, W. & Nitsche, R. (1974). *Mater. Res. Bull.* **9**, 645–654.

Schnabel, T., Seboui, M. & Ahlswede, E. (2017). *Energies*, **10**, 1813.

Schorr, S. (2011). *Sol. Energy Mater. Sol. Cells*, **95**, 1482–1488.

Schorr, S., Hoebler, H. & Tovar, M. (2007). *Eur. J. Mineral.* **19**, 65–73.

Többens, D. M., Gunder, R., Gurieva, G., Marquardt, J., Neldner, K., Valle-Rios, L. E., Zander, S. & Schorr, S. (2016). *Powder Diffraction*, **31**, 168–175.

Többens, D. M., Gurieva, G., Levcenko, S., Unold, T. & Schorr, S. (2016). *Phys. Status Solidi B*, **253**, 1890–1897.

Villars, P. & Cenzual, K. (2019). *Pearson's Crystal Data: Crystal Structure Database for Inorganic Compounds.* Materials Park, Ohio, USA: ASM International.

Wojdyr, M. (2010). *J. Appl. Cryst.* **43**, 1126–1128.

Wong, J. (2018). *Reference X-Ray Spectra of Metal Foils*, http://exafsmaterials.com/Ref_Spectra_0.4MB.pdf.

Yao, G. Q., Shen, H. S., Honig, E. D., Kershaw, R., Dwight, K. & Wold, A. (1987). *Solid State Ionics*, **24**, 249–252.

Zhang, L., Wang, J., Li, J. K., Schuck, G., Winter, M., Schumacher, G. & Li, J. (2020). *Nano Energy*, **70**, 104535.